The Astrophysical Journal, 621:498–511, 2005 March 1
© 2005. The American Astronomical Society. All rights reserved. Printed in U.S.A.

MAGNETIC PROPERTIES AT FOOTPOINTS OF HOT AND COOL LOOPS

Yukio Katsukawa and Saku Tsuneta
National Astronomical Observatory of Japan, 2-21-1 Osawa, Mitaka, Tokyo 181-8588, Japan; yukio.katsukawa@nao.ac.jp
Received 2004 May 25; accepted 2004 November 17

ABSTRACT

Observations of the solar corona with *Yohkoh*, the *Solar and Heliospheric Observatory*, and the *Transition Region and Coronal Explorer* (*TRACE*) have revealed that individual coronal loops of active regions have their own temperatures from 1 to 5 MK. The hot (2–5 MK) Soft X-Ray Telescope (SXT) loops appear to require more heating energy than the cool (1–2 MK) EUV loops. We investigate the photospheric magnetic signature for the hot and cool loops with the Advanced Stokes Polarimeter. In contrast to the cool loops, the hot loops observed with the SXT are usually diffuse, resulting in ambiguous identification of their footpoint locations. We use *TRACE* "moss" structure, which we confirm is low-lying EUV emission at the footpoints of the hot loops. Footpoints of both loops have magnetic fields whose strength is 1.2–1.3 kG, and the orientation is almost vertical to the surface. A significant difference is discovered in the magnetic filling factor, which is defined by the fraction of a pixel filled with a magnetized atmosphere. The footpoints of the hot loops have a lower filling factor than the footpoints of the cool loops. We suggest that braiding of coronal magnetic fields is more efficient at the footpoints of the hot loops than at the footpoints of the cool loops as a result of the combination of the lower filling factor and higher horizontal velocity.

Subject headings: Sun: corona — Sun: magnetic fields — Sun: photosphere — Sun: UV radiation

Online material: color figure

1. INTRODUCTION

The solar corona is highly inhomogeneous and structured, and its building blocks are loops representing closed magnetic flux tubes. With the Soft X-ray Telescope (SXT) aboard *Yohkoh*, the Extreme Ultraviolet Imaging Telescope (EIT) aboard the *Solar and Heliospheric Observatory* (*SOHO*), and the *Transition Region and Coronal Explorer* (*TRACE*), it becomes clear that individual coronal loops have different temperatures. On the basis of *Yohkoh*-SXT observations, Yoshida & Tsuneta (1996) show that the temperature of the quasi-stationary active region ranges from 3 to 5 MK, while its high-temperature ($T > 5$ MK) portion is transiently heated. Observations with the EIT and *TRACE* show that there are also a large number of low-temperature ($T \sim 1$–2 MK) stationary loops in active regions (e.g., Schrijver et al. 1999). Hot loops, whose temperatures are greater than 2 MK, are observed with broadband soft X-ray telescopes such as the SXT, whereas cool loops, whose temperatures are 1–2 MK, are observed with narrowband (frequently used wavelengths are Fe IX/X 171 Å and Fe XII 195 Å) EUV telescopes such as *TRACE*. Nagata et al. (2003) clearly show that the hot loops seen in SXT images and the cool loops seen in EIT images are located in a spatially exclusive way.

The hot and cool loops have different properties. The temperatures, lengths, and pressures of the hot loops generally conform to the theoretical predictions of the Rosner-Tucker-Vaiana (Rosner et al. 1978) scaling laws (Kano & Tsuneta 1995; Yashiro & Shibata 2001). The temperature and density distributions along individual hot loops were studied by Kano & Tsuneta (1996) and Priest et al. (1998, 2000). Those loops have a significant temperature increase from their feet to their summits; thus, the heating source must be located in the upper portion of the loops. Kano & Tsuneta (1996) also report that the emission measure is highest around the loop top and decreases toward the footpoints. They estimate that the energy flux to heat the hot loops is larger than 1×10^7 ergs cm^{-2} s^{-1} for the loops whose lengths are about 10^{10} cm. The density and temperature distributions along individual cool loops have been studied by several authors using the EIT and *TRACE* (Lenz et al. 1999; Reale & Peres 2000; Aschwanden et al. 2000, 2001; Winebarger et al. 2003). They report nearly flat temperature profiles along the loops, suggesting that heating is concentrated near their footpoints. The heating energy for the cool loops is estimated to be around 1×10^6 ergs cm^{-2} s^{-1} (Aschwanden et al. 2001).

The relationship between the coronal X-ray emission and the photospheric magnetic fields has been investigated by some authors. Fisher et al. (1998) and Yashiro & Shibata (2001) found a correlation between coronal properties observed with the SXT and photospheric magnetic flux for many active regions. These works are based on physical quantities integrated over each active region and imply that the relation between the heating flux F and the magnetic flux B can be roughly expressed as $F \propto B^{\alpha}$, where $\alpha \sim 1$ (Yashiro & Shibata 2001). But it is known that strong magnetic fields do not always result in large energy input to the corona. The most significant example is the corona directly above a sunspot umbra, where soft X-ray intensities are remarkably small (Vaiana et al. 1976; Pallavicini et al. 1979; Vourlidas et al. 1997). Not only the magnetic flux but other factors would contribute to the coronal heating. Falconer et al. (1997) report that the bright structures observed with the SXT have feet near regions with strong magnetic shear, and they suggest the importance of electric currents for the heating of the hot loops.

In this paper we investigate the photospheric magnetic fields of coronal loops—in particular, the hot and cool loops. There is little ambiguity in the determination of the footpoint positions for the cool loops observed with *TRACE*, because the loops have a sharp appearance and the EUV intensity increases toward their footpoints (Schrijver et al. 1999; Aschwanden et al. 2001). However, the identification of the footpoints for the hot loops observed with the SXT has larger uncertainties in position, because the hot loops have a fuzzy appearance and the

TABLE 1
SUMMARY OF SXT AND *TRACE* DATA

Image	Date	Start	End	Exposure	Number of Images
TRACE 171 Å.....	2000 Nov 19	16:56:28 UT	16:59:09 UT	32.8 s	5
SXT Al.1	2000 Nov 19	16:08:08 UT	16:31:04 UT	168 ms	3

intensity becomes faint toward the footpoints in soft X-rays (Kano & Tsuneta 1996). EUV observations with *TRACE* revealed that there is a low-lying ~1 MK bushy structure ("moss") at the base of the hot loops (Berger et al. 1999; Fletcher & de Pontieu 1999; see also Yoshida et al. 1995). The moss structure may be produced by conductive heat flux from the hot (>3 MK) and high-pressure plasma (Martens et al. 2000). We thus employ the moss structure as a fiducial of the base of the hot loops.

The identification of the footpoint locations for the hot and cool loops is critically important to investigate magnetic properties at and around the footpoints of these loops. We employ the Advanced Stokes Polarimeter (ASP) at the National Solar Observatory to perform a precise measurement of the vector magnetic fields in the photosphere. The ASP observation provides us with not only a longitudinal component of the magnetic flux but three-dimensional vectors of magnetic fields by full spectral and polarimetric coverage. Doppler velocities, magnetic filling factors, and some thermodynamic quantities can also be derived with the ASP.

2. OBSERVATION AND DATA ANALYSIS

We carried out a cooperative observation of the NOAA AR 9231 from 2000 November 14 to 22 with the SXT (Tsuneta et al. 1991) aboard the *Yohkoh* satellite (Ogawara et al. 1991), the Michelson Doppler Imager (MDI; Scherrer et al. 1995) aboard *SOHO*, *TRACE* (Handy et al. 1999), and the ASP at the National Solar Observatory (Elmore et al. 1992; Lites 1996). Here we use only the data taken on November 19, because seeing is moderate and the target region is located near the central meridian on that day.

2.1. *Coronal Observation*

TRACE obtained 171 Å images every 40 s during the ASP observation with an exposure time of 32.8 s. The 171 Å images are dominated by emission lines from Fe IX and Fe X, which are formed at a temperature of around 1 MK (Handy et al. 1999). Although emissions from O VI ($T \sim 0.3$ MK) and Fe XXIII ($T \sim 10$ MK) are also included in the *TRACE* 171 Å band, their contributions are 1–2 orders of magnitude smaller than those of Fe IX/X (Nagata et al. 2003). The *TRACE* data were processed with the standard software available in the Solar Software (SSW) package. The procedure performed dark and pedestal subtraction and flat-fielding. Bad pixels due to cosmic-ray hits were also removed by the median filter, which replaced a spiky pixel by the local median value. Although the procedure did not completely remove damaged pixels in heavily damaged data, we chose less damaged images by checking the median-filtered data and confirmed that the effect of the cosmic-ray hits was negligible for this study. The *TRACE* 171 Å image presented below was created by summing five images. The observation time, exposure duration, and number of images used in summation are summarized in Table 1.

The *Yohkoh*-SXT observed the corona through Al.1 and Al12 filters alternatively. During the ASP observation, the cadence was not so high, and four to five images for each filter were taken per orbital period of the satellite. The soft X-ray image presented in this paper was created by summing a few images obtained through the Al.1 filter during one orbital period. The SXT data used in this paper are summarized in Table 1.

2.2. *ASP Observation*

The data of photospheric vector magnetic fields were obtained with the ASP at the Dunn Solar Telescope at Sacramento Peak. The data consist of spatially resolved full Stokes profiles of the spectral lines Fe I $\lambda\lambda$6301.5 and 6302.5 with 12 mÅ pixel^{-1} dispersion and 230 pixels (0.″37 pixel^{-1}) in spatial dimension along the slit. The spectrograph slit was stepped across a region of interest on the solar disk with step size chosen by the observer. In this observation, the step size was 0.″525. It took about 30 minutes to complete each scan with around 300 steps in total. Since the target active region, NOAA AR 9231, was elongated along the east-west direction, the entire region was covered with mosaic observations. On November 19, the region was observed with two scans. The calibration of the obtained ASP data was performed by the method described in Skumanich et al. (1997). The observation time, pointing, and number of steps of the data used in this analysis are summarized in Table 2.

We performed the Stokes inversion using the nonlinear least-squares fit based on the Unno-Rachkovsky solution developed by the High Altitude Observatory (HAO; Skumanich & Lites 1987; Lites & Skumanich 1990). This HAO inversion code fits the Stokes profiles with two contribution functions, one from a magnetic atmosphere and the other from a nonmagnetic atmosphere. Using this assumption, the observed Stokes profile (I, Q, U, V) is given by

$$\begin{pmatrix} I \\ Q \\ U \\ V \end{pmatrix} = f \begin{pmatrix} I^{\rm mag} \\ Q^{\rm mag} \\ U^{\rm mag} \\ V^{\rm mag} \end{pmatrix} + (1-f) \begin{pmatrix} I^{\rm nmag} \\ 0 \\ 0 \\ 0 \end{pmatrix}, \qquad (1)$$

where $I^{\rm mag}$ is the intensity from the magnetic atmosphere, $I^{\rm nmag}$ is the intensity from the field-free atmosphere, and f is a magnetic filling factor. The inversion code assumes a Milne-Eddington model for the magnetized atmosphere so that one value of the magnetic field vector is derived in each ASP pixel. The least-squares fit to the Stokes profiles gives the vector field in the observer's reference frame with the z-axis aligned with the line of sight. The derived magnetic field vectors are then

TABLE 2
SUMMARY OF ASP DATA

Date	Start	End	Step	FOV Center (arcsec)
2000 Nov 19.....	16:09:53 UT	16:40:39 UT	310	(160, −410)
2000 Nov 19.....	16:51:59 UT	17:21:38 UT	300	(14, −453)

translated into vectors in the local reference frame with the z-axis aligned with the normal to the solar surface. In this local reference frame, the vector field is represented by ($|B|$, γ, χ), where $|B|$ is the intrinsic magnetic field strength and γ represents the inclination angle between the magnetic field and the normal to the solar surface (zenith angle). The relation $\gamma = 0^\circ$ means that the magnetic field is vertical and outward to the surface, and $\gamma = 180^\circ$ means that the magnetic field is vertical and inward to the surface. When the magnetic field is parallel to the surface, γ is 90°. The azimuth angle with 0° given by the local solar west direction is represented by χ. The 180° ambiguity in the azimuth angle was resolved by the interactive AZAM procedure (written in IDL by P. Seagraves; Lites et al. 1995). The Stokes inversion was performed for all the points at which the degree of polarization, which is defined as $p = (Q^2 + U^2 + V^2)^{1/2}/I$ integrated over the 6302.5 Å line, is above 0.4%. The Stokes I profile of the nonmagnetic component, $I^{\rm nmag}$, was computed from the profile averaged over the spatial pixels with a degree of polarization below 0.28%. We also use the continuum intensity I_c around 6303 Å. The value of I_c is defined here as the ratio with respect to the continuum intensity averaged over the spatial pixels where the degree of polarization is less than 0.28%.

From the vector fields obtained with the ASP, we calculated the electric currents normal to the surface, J_z, using the formula

$$J_z = \frac{1}{\mu}\left(\frac{\partial B_y}{\partial x} - \frac{\partial B_x}{\partial y}\right), \tag{2}$$

where J_z is in units of A m^{-2} and $\mu = 4\pi \times 10^{-3}$ G mA^{-1} is the magnetic permeability. The variable x denotes the local solar west and y the local solar north. Here B_x and B_y represent the magnetic flux (averaged in each ASP pixel) directed to the local solar west and north, respectively, and are given by

$$\begin{pmatrix} B_x \\ B_y \end{pmatrix} = f|B| \sin\gamma \begin{pmatrix} \cos\chi \\ \sin\chi \end{pmatrix}, \tag{3}$$

where χ and γ are the local azimuth and inclination, respectively. We used the ambiguity-free method in the above calculation of the electric currents (Semel & Skumanich 1998) to avoid a nonrealistically large current in azimuth discontinuity.

2.3. *Image Co-Alignment*

The coronal data obtained with the SXT and *TRACE* were aligned with the photospheric data obtained with the MDI and the ASP to investigate the correspondence between the photosphere and the corona. All the data have information about the field-of-view (FOV) center position relative to the Sun center, and we used this for coarse alignment. Fine pointing was done with the following procedure.

The precise pointing for the *TRACE* data relative to the Sun center and the roll angle relative to the solar north were obtained through the EIT (Delaboudinière et al. 1995). The pointing information of the EIT has been well calibrated by fitting the limb of the full solar disk. The EIT 195 Å image nearest in time to the *TRACE* 171 Å data was used to obtain the pointing error of the *TRACE* data by maximizing cross-correlation coefficients.

The ASP data were aligned with a longitudinal magnetogram obtained with the MDI. The MDI data also have accurate pointing information owing to their full-disk observations. Longitudinal magnetograms similar to those of the MDI were generated from the vector magnetic field maps obtained with the ASP. The pointing errors of the ASP vector field maps were obtained by maximizing cross-correlation coefficients with the MDI magnetogram. The alignment accuracy between the photospheric data obtained with the ASP and the coronal data obtained with *TRACE* and the SXT is estimated to be within $1''-2''$.

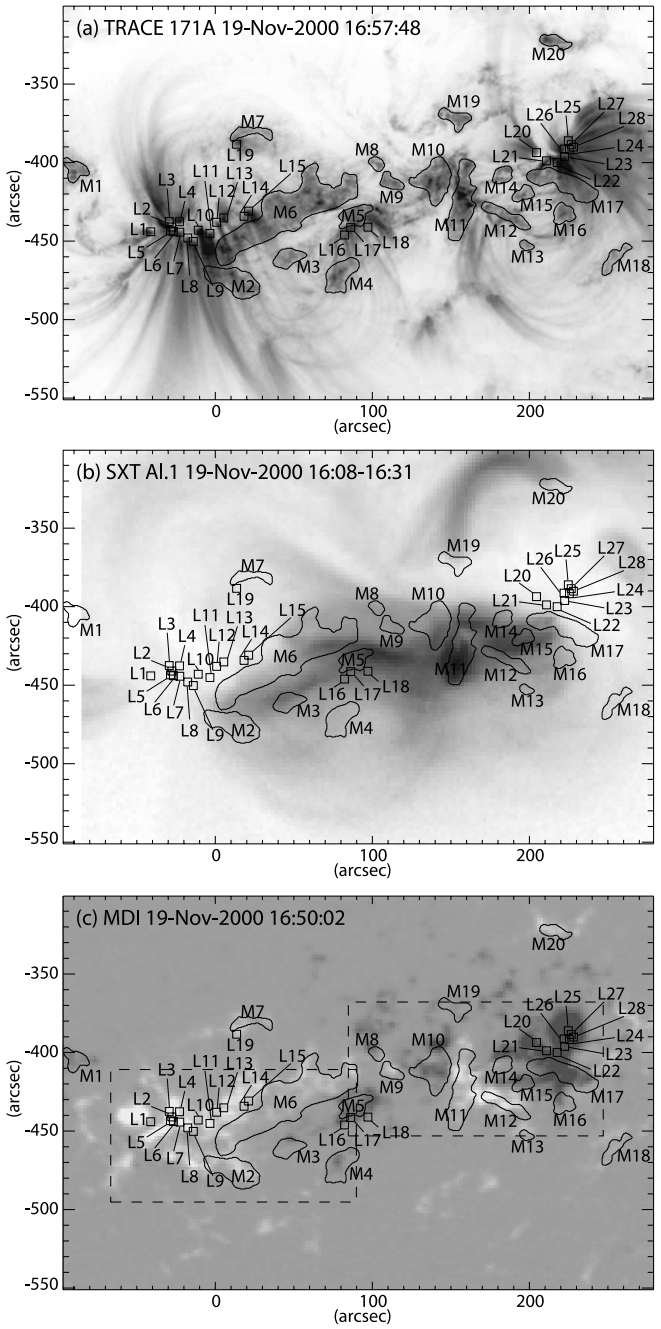


FIG. 1.—(*a*) *TRACE* 171 Å image, (*b*) SXT Al.1 image, and (*c*) MDI longitudinal magnetogram of 2000 November 19. Moss regions are encircled with solid curves. Squares show footpoint regions of the cool loops. The dashed rectangles on the MDI map (*c*) show the region observed with the ASP. [*See the electronic edition of the Journal for a color version of this figure.*]

3. SPATIAL DISTRIBUTION OF HOT AND COOL LOOPS

Figure 1 shows NOAA AR 9231 observed with *TRACE*, *Yohkoh*-SXT, and the MDI on 2000 November 19. Figure 2 shows the continuum intensity and magnetic flux maps of the active region obtained with the ASP. The active region had a

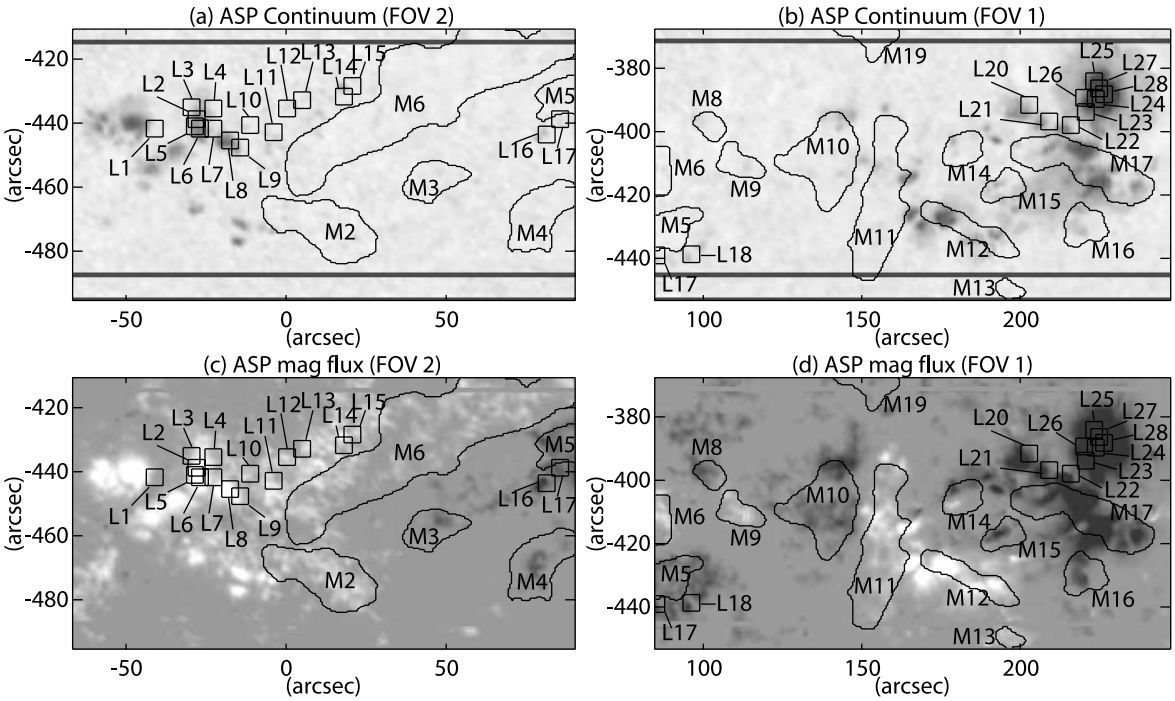


FIG. 2.—Maps obtained with the ASP on 2000 November 19. Panels (*a*) and (*b*) show the continuum intensity maps, and panels (*c*) and (*d*) show the magnetic flux maps. The active region was almost covered with two scans.

rapidly growing emerging flux region on the southeastern side of the leading sunspot, and the evolution of the emerging region was studied by Kubo et al. (2003) using the ASP.

3.1. *Moss Regions and Hot Loops*

The moss regions, which are footpoints of hot loops, are selected using the following procedure. The *TRACE* 171 Å image is smoothed with a boxcar average of the 5 pixel (corresponding to 2.″5) window. Then we mask the pixels in which the intensity is less than 5 DN s^{-1} $pixel^{-1}$ (DN is the data number of TRACE). The criterion of 5 DN s^{-1} $pixel^{-1}$ corresponds to the emission measure of about 9×10^{26} cm^{-5} when we use half-width at half-maximum of the temperature response function (Handy et al. 1999). Only the regions in which the low-lying patchy structure, i.e., moss, can be seen are extracted by visual inspection. We further remove the regions composed of fewer than 150 pixels (corresponding to about 2×10^{17} cm^2) in order to use only significant moss regions in the following analysis. We identify 20 moss regions in the *TRACE* image on 2000 November 19, and the regions are encircled by solid curves in Figures 1 and 2. The area of each moss region is listed in Table 3.

We notice that the moss regions thus identified are located at approximately the footpoints of the bright loops observed with the SXT. The clearest examples are M19 and M20, located at both ends of a bright SXT loop. Many SXT loops emanate from the large moss regions M2 and M6 and enter into M5, M10, and M17. Bright, compact SXT loops are visible between M11/M12 and M17. Small moss regions M14 and M15 are located below the compact SXT loops.

3.2. *Footpoints of Cool Loops*

Cool loops observed with the *TRACE* 171 Å band are extracted by visual inspection. The intensities of the cool loops in the *TRACE* 171 Å image increase along the loops toward footpoints (e.g., Aschwanden et al. 2001; Winebarger et al. 2003), and the identification of the footpoint location is easier and much less ambiguous than in the hot loops observed with the SXT. We only use the loops that meet the condition that the 171 Å intensities around the footpoints are greater than 10 DN s^{-1} $pixel^{-1}$ (corresponding to the emission measure of about 2×10^{27} cm^{-5}). Taking into account uncertainties in the identification of the footpoints and the co-alignment of the images, the footpoint region for each loop is defined by a square box of 5″ (corresponding to 10 pixels in the *TRACE* image) centered on each identified footpoint position. Typical loop width near its footpoint is about 3″, and the 5″ window used here is slightly larger than the loop width.

The 28 footpoints of cool loops are extracted from the *TRACE* image of 2000 November 19 and are indicated by the squares in Figures 1 and 2. The loops seen in the *TRACE* 171 Å image have the footpoints around the main sunspots at the east and west ends of the active region. In particular, many loops are extended from the leading sunspot and form a fanlike structure (Schrijver et al. 1999) above the spot. It is clear that all the footpoint regions identified in the *TRACE* image are located in the regions in which the soft X-ray intensities are small in the SXT image (Fig. 1*b*).

4. MAGNETIC PROPERTIES IN THE MOSS REGIONS

4.1. *Moss Regions*

Properties of the photospheric magnetic fields at the *TRACE* moss regions are investigated using the data obtained with the ASP (see Fig. 2). When we map the regions of interest in the *TRACE* image to the photospheric maps obtained with the ASP, the height difference between the corona observed with *TRACE* and the photosphere has to be taken into account. When a region is located at $(x,\ y)$ (in units of arcseconds) relative to the Sun center, the height difference h causes a positional shift,

$$(\delta x,\ \delta y) = \frac{h}{R_\odot}(x,\ y), \tag{4}$$

TABLE 3
PROPERTIES OF THE MOSS REGIONS ON 2000 NOVEMBER 19

Number (1)	Area (10^{17} cm^2) (2)	Valid (%) (3)	NS or EFR (4)	γ (deg) (5)	$\lvert B\rvert$ (kG) (6)	f (7)	I_c (8)	$p_{\rm mix}$ (9)	$\lvert J_z\rvert$ (mA m^{-2}) (10)
M1	7.8	...	...	...	...	...	...	...	...
M2	23.7	92.7	NS	22.1	1.16	0.305	1.004	0.000	4.15
M3	9.2	64.3	NS	151.5	1.20	0.158	0.997	0.022	2.82
M4	16.0	62.8	NS	165.8	1.22	0.168	1.002	0.000	2.99
M5	10.8	100.0	NS	168.0	1.27	0.305	1.006	0.000	3.63
M6	99.6	89.8	NS	15.2	1.20	0.173	1.008	0.002	2.61
M7	7.3	...	...	...	...	...	...	...	...
M8	3.4	95.2	NS	145.2	1.31	0.287	0.989	0.068	3.74
M9	5.7	90.5	NS	18.2	1.23	0.236	1.000	0.000	3.49
M10	23.5	95.2	NS	160.5	1.26	0.294	0.986	0.001	3.44
M11	30.0	97.0	NS	14.7	1.26	0.244	0.975	0.000	3.41
M12	10.1	99.7	EFR	37.3	1.38	0.682	0.816	0.000	8.23
M13	2.2	99.5	NS	16.5	1.16	0.314	1.012	0.000	2.71
M14	5.7	99.1	EFR	104.7	0.92	0.535	0.971	0.426	6.59
M15	5.2	100.0	EFR	122.9	0.96	0.684	0.920	0.020	11.36
M16	7.3	98.0	EFR	131.6	1.06	0.485	0.935	0.000	6.07
M17	25.3	100.0	EFR	145.4	1.47	0.707	0.786	0.000	7.89
M18	7.2	...	...	...	...	...	...	...	...
M19	8.2	60.6	NS	168.2	1.19	0.069	1.012	0.000	3.27
M20	6.3	...	...	...	...	...	...	...	...

NOTE.—See Fig. 1.

where $R_\odot$ is the solar radius. Berger et al. (1999) and Martens et al. (2000) measured the height of the moss above the photosphere using a limb observation and found that the average height was 2800 km. Here we correct the positional shift due to the height difference corresponding to $h = 3000$ km for each moss region.

The intrinsic field strength $|B|$, the inclination of the magnetic field γ, the magnetic filling factor f, the continuum intensity I_c, and the normal component of the electric current J_z are measured with the ASP for each moss region. The mean values of the parameters are calculated in each region and tabulated in Table 3. The magnetic parameters cannot be examined for a few moss regions in the outside of the ASP field of view. There are some pixels for which we cannot obtain the magnetic parameters because of low polarization signal in the moss regions. The percentage of valid data pixels in which the degree of polarization is larger than 0.4% is listed in column (3) of Table 3. We classify the moss regions into two types in terms of their magnetic properties as listed in column (4) of Table 3: those in nonsunspot (NS) regions and those associated with the emerging flux region (EFR). The magnetic properties for the moss regions associated with the emerging flux are described in the next subsection. No moss region is found above the sunspots.

The moss regions in NS regions have magnetic fields whose strength is 1.16–1.31 kG, and the orientation is nearly vertical to the solar surface ($\gamma < 30^\circ$ or $\gamma > 150^\circ$) as the averaged values listed in Table 3. The continuum intensities in the moss regions are nearly 1.0. Figure 3 shows typical histograms of the magnetic parameters $|B|$, γ, and f for the NS moss regions M2, M6, M10, and M19. All the histograms of the field strength exhibit a similar appearance and have a clear peak between 1.0 and 1.5 kG. The histograms of the inclination indicate that the magnetic fields tend to have a vertical orientation for all the regions. The averaged magnetic filling factor ranges from 0.069 to 0.314 in Table 3. The histograms of the filling factor in Figure 3 exhibit somewhat broad distributions but show that the moss regions are dominated by the pixels whose filling factor is less than 0.4. These characteristics of magnetic fields are similar to those of magnetic fields observed in plages (Martinez Pillet et al. 1997).

4.2. *Moss Regions Associated with Flux Emergence*

The moss regions M14, M15, and M16 are located below the compact and bright SXT loops on the southeast side of the large leading spot and are not apparent footpoints of hot loops. Flux-emerging events are identified by Kubo et al. (2003) in these regions. The regions have slightly weak field strength (less than 1.1 kG), and the inclination of the field is large (greater than 45°), as shown in Table 3. Figure 4 shows the histograms in the moss regions M14 and M15. These regions have two magnetic components. One is the magnetic field whose strength is 1.0–1.7 kG and is nearly vertical to the solar surface ($\gamma < 30^\circ$ or $\gamma > 150^\circ$). The other is the magnetic field nearly parallel to the solar surface ($\gamma \sim 90^\circ$) and weak ($|B| \sim 500$ G). They are the characteristics of EFRs (Lites et al. 1998; Kubo et al. 2003). The low-lying EUV structure in these regions does not seem to be pure moss located at the feet of the hot loops. It appears that the small low-lying loops just emerged look like the moss defined in this paper (see also Martens et al. 2000).

The moss regions M12 and M17 are located at both ends of the EFR and are roughly coincident with the feet of the compact and bright SXT loops above the emerging flux. The conjugate regions M12 and M17 are found to be in penumbral regions in the continuum intensity maps in Figure 2. The histograms in Figure 4 exhibit clearly different properties from the normal moss regions shown in Figure 3. The magnetic field strength ranges from 0.5 to 2.2 kG in the regions and has a broader distribution. The inclination is larger than that of the normal moss regions. The pixels whose filling factors are large (0.6–0.9) dominate those regions.

The electric currents $|J_z|$ shown in Table 3 have relatively larger values in M12 and M17 than in the other moss regions.

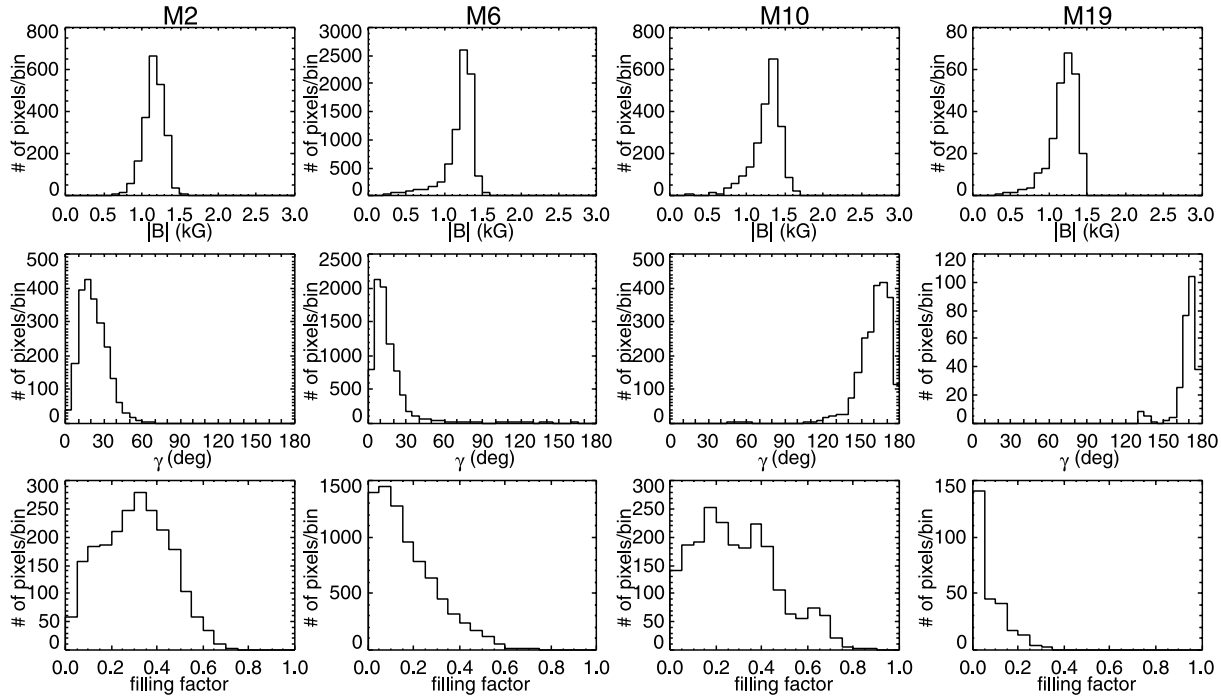


FIG. 3.—Histograms of the magnetic field strength $|B|$ (*top*), the magnetic field inclination γ (*middle*), and the filling factor f (*bottom*) for the moss regions M2, M6, M10, and M19 (*left to right*).

Figure 5 shows the histograms of the electric currents J_z for the moss regions M6, M10, M12, and M17. It is clear that the electric currents in the moss regions associated with the conjugate emerging flux bipoles (M12 and M17) have large dispersions. In addition, the electric current averaged over each region has a little offset to zero, although the offset is much smaller than the dispersion. The averaged electric currents are -2.8 and $+2.3$ mA m^{-2} in M12 and M17, respectively. The opposite signs of J_z suggest that the electric currents are flowing from M17 to M12. The electric currents in the moss regions M6 and M10 have much smaller dispersions, and the averaged currents are nearly zero.

Figure 6 shows averaged *TRACE* 171 Å intensities as a function of time for the NS moss regions (M3, M5, M18, and M20) and the EFR moss regions (M12, M14, M15, and M17). The fluctuation of the intensity is small in many moss regions, as shown in the upper panels of Figure 6 (Antiochos et al. 2003). On the other hand, the moss regions associated with the EFR

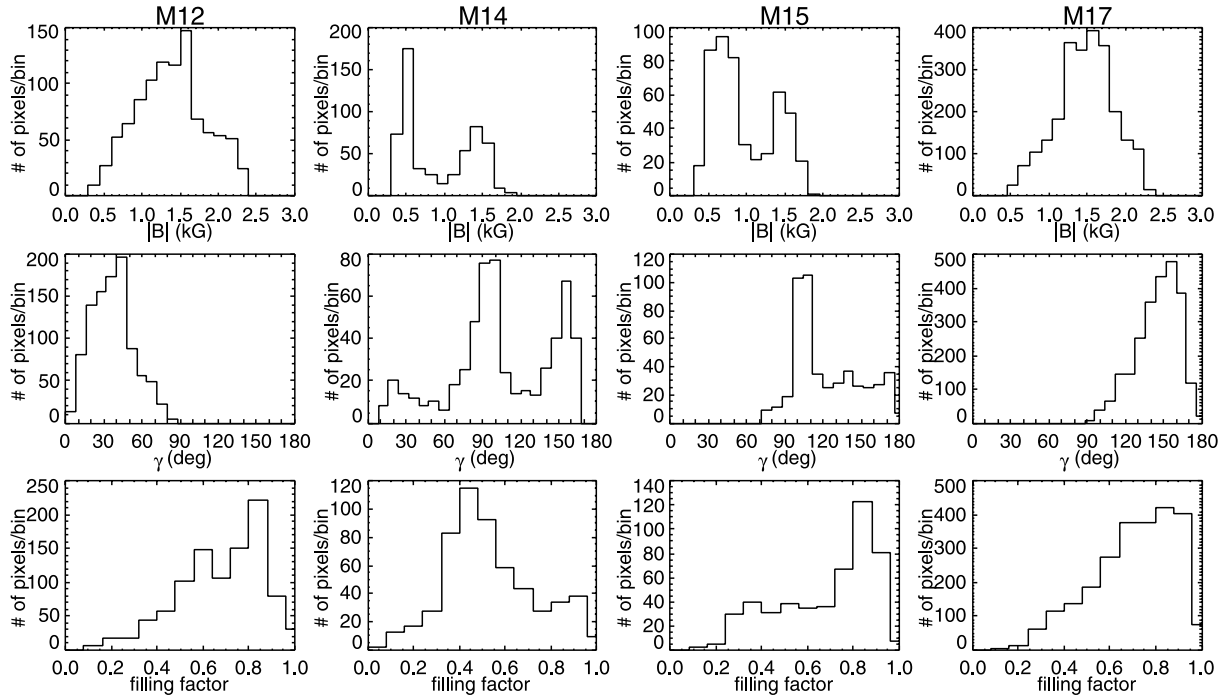


FIG. 4.—Same as Fig. 3, but for the moss regions M12, M14, M15, and M17 (*left to right*).

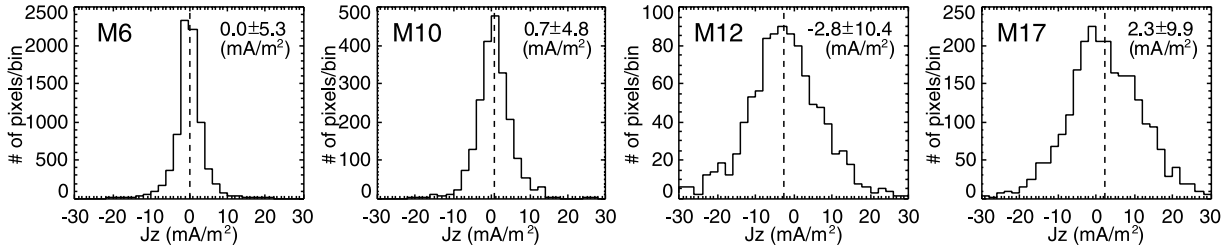


FIG. 5.—Histograms of the electric currents J_z for the normal moss regions (M6 and M10) and those associated with the emerging flux (M12 and M17). The vertical dotted lines indicate a mean value for each moss region, and the mean and the standard deviation are shown in the upper right corner of each histogram.

have larger variabilities. The moss regions M14 and M15 at the center of the EFR have many spikes with short duration. This may correspond to the emergence of small low-lying loops. The moss region M12 on the penumbra does not have such short spikes, but it has a significant intensity enhancement between 17:20 and 17:30 UT caused by a microflare. Berger et al. (1999) reported an example of the moss associated with a flare. Although major flares did not occur during the period of this observation, the moss region M12 that has the higher EUV variability and the slightly large electric current might be associated with hot coronal plasma produced by transient events (see also Schmieder et al. 2004).

4.3. *Mixed Polarity*

The degree of mixed polarity $p_{\rm mix}$ is defined as

$$p_{\rm mix} = 1 - \left| \frac{|\Phi_+| - |\Phi_-|}{|\Phi_+| + |\Phi_-|} \right|, \qquad (5)$$

where $|\Phi_\pm|$ means the absolute value of the total magnetic flux with $\pm$ polarity. The plus polarity corresponds to $\gamma < 90^\circ$, and the minus polarity corresponds to $\gamma > 90^\circ$. In this definition $p_{\rm mix} = 0$ if the magnetic flux in a region is fully inclined to one polarity, and $p_{\rm mix} = 1$ if the region has the same amount of magnetic flux with plus and minus polarities.

Table 3 shows that all the moss regions except M14 have $p_{\rm mix} \simeq 0$ and are essentially of single polarity. Since M14 is the region in which the magnetic fields are nearly parallel to the solar surface, as described in § 4.2, such high $p_{\rm mix}$ is related to this. Sánchez Almeida et al. (2003) performed simultaneous infrared and visible spectropolarimetric observations of a solar internetwork region in the quiet Sun and showed the cores that have visible and infrared Stokes V profiles with opposite polarity in one resolutional element (see also Lites 2002). We have shown that the majority of pixels in most of the moss regions have the same polarity. This does not exclude the possibility that a small number of magnetic fields with opposite polarities coexist in a resolutional element.

5. MAGNETIC PROPERTIES AT THE FOOTPOINTS OF THE COOL LOOPS

The magnetic properties obtained with the ASP are examined in the same way as the moss regions for the loop footpoint regions determined in § 3.2. The height difference between the photosphere and the corona is also corrected according to equation (4) with $h = 3000$ km when we map the footpoints of the *TRACE* loops onto the ASP maps.

The averaged values for the magnetic field strength $|B|$, the magnetic inclination γ, the magnetic filling factor f, and the continuum intensity I_c are listed in Table 4. We classify the footpoint regions into two types in terms of whether the footpoint is situated on a sunspot (S) or not (NS), as shown in Table 4. About two-thirds of the loop footpoints are located on the sunspots, and one-third are located in the NS regions. The percentage of valid pixels for which the degree of polarization is larger than 0.4% is 100% for all the footpoint regions and is not shown in Table 4. The degree of mixed polarity defined by equation (5) is 0 for all the footpoint regions, and no mixed polarity is observed there.

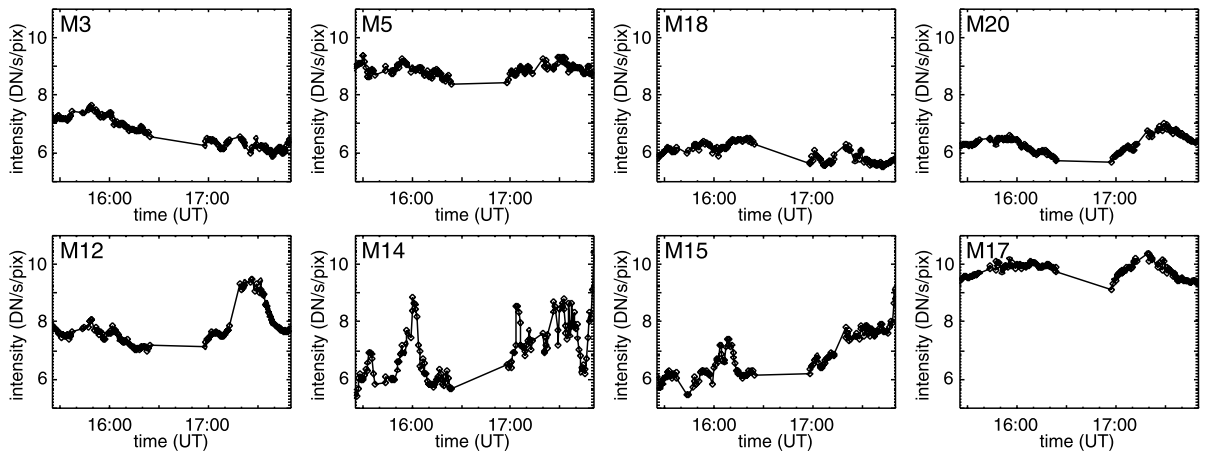


FIG. 6.—Intensities observed with *TRACE* 171 Å as a function of time for the NS moss regions (*top*; M3, M5, M18, and M20) and the regions associated with the emerging flux (*bottom*; M12, M14, M15, and M17). The intensities represent the averaged value in each region. For an unknown reason, there is a data gap from 16:25 to 16:55 UT.

TABLE 4
PROPERTIES OF THE LOOP FOOTPOINT REGIONS ON 2000 NOVEMBER 19

Number	Sunspot or NS	γ (deg)	$\lvert B\rvert$ (kG)	f	I_c	$\lvert J_z\rvert$ (mA m^{-2})
L1	S	51.2	0.91	0.464	0.928	6.13
L2	S	26.7	1.60	0.752	0.733	7.85
L3	S	43.4	1.21	0.502	0.905	5.54
L4	S	28.5	1.36	0.445	0.935	5.51
L5	S	23.6	1.68	0.771	0.709	6.94
L6	S	16.3	1.72	0.801	0.676	6.20
L7	S	22.0	1.50	0.522	0.875	6.47
L8	S	24.5	1.66	0.753	0.679	7.46
L9	S	30.8	1.31	0.600	0.862	5.09
L10	NS	13.6	1.33	0.323	0.992	2.58
L11	NS	12.8	1.36	0.436	0.968	4.63
L12	NS	10.6	1.28	0.342	0.982	2.65
L13	NS	17.9	1.31	0.312	0.993	4.39
L14	NS	11.9	1.30	0.400	0.972	3.52
L15	NS	13.6	1.31	0.394	0.975	3.24
L16	NS	158.3	1.38	0.408	0.950	5.57
L17	NS	170.3	1.36	0.418	0.973	3.83
L18	NS	159.6	1.38	0.375	0.938	6.49
L19	NS	...	...	...	...	...
L20	S	140.0	1.38	0.604	0.852	11.10
L21	S	152.5	1.52	0.485	0.852	8.62
L22	S	144.7	1.50	0.649	0.795	11.48
L23	S	154.1	1.91	0.881	0.563	4.28
L24	S	165.9	2.43	0.964	0.289	5.22
L25	S	156.0	2.25	0.949	0.353	9.73
L26	S	150.1	2.09	0.906	0.491	6.14
L27	S	165.0	2.51	0.965	0.250	11.16
L28	S	168.2	2.63	0.970	0.233	3.84

NOTE.—See Fig. 1.

5.1. *Footpoints in the Nonsunspot Regions*

Figure 7 shows typical histograms of the magnetic parameters $|B|$, γ, f, and I_c in the NS loop footpoint regions L10, L12, L15, and L17. The averaged properties tabulated in Table 4 and the histograms in Figure 7 show that all the footpoints of NS regions have similar magnetic properties: the magnetic field strengths $|B| \sim 1.3$–1.4 kG; the magnetic inclinations $\Delta\gamma \sim 10^\circ$–$22^\circ$ (nearly vertical to the surface), where $\Delta\gamma = \gamma$ when $\gamma < 90^\circ$ and $\Delta\gamma = (180^\circ - \gamma)$ when $\gamma > 90^\circ$; and the magnetic filling factors $f \sim 0.31$–0.44, as shown in Table 4. It is clear that the filling factor is larger than 0.2 in Figure 7. The continuum intensities I_c are clearly smaller than 1. Figure 8 shows the scatter plots of the continuum intensity, field strength, and inclination as a function of the magnetic filling factor for the footpoints in the NS regions. As the filling factors become greater than about 0.4, the continuum intensities become less than unity. Simultaneously, the magnetic field strengths become greater than 1.2 kG.

When magnetic elements are concentrated enough in the photosphere, the continuum intensity decreases, and pores are formed as a result (e.g., Sobotka et al. 1999; Berger & Title 2001). Leka & Skumanich (1998) studied the process of the pores' formation with the ASP and found that a magnetic flux of $\simeq 2\times10^{19}$ Mx corresponded to the initial formation of pores. The magnetic properties for the footpoint regions clearly correspond to pores. We note that the observed continuum intensities in the pores are affected by the scattering from the surrounding area (Keppens & Martinez Pillet 1996). Actual continuum intensities in the pores are probably about 10% smaller than the observed value based on the estimation by Keppens & Martinez Pillet (1996). The scattering from the surrounding area may tend to decrease the magnetic filling factor in the pores because the surrounding regions with normal brightness generally have smaller filling factors.

5.2. *Footpoints in the Sunspots*

Figure 9 shows histograms of the magnetic parameters in the sunspot footpoint regions L3, L7, L20, and L25. It is difficult to find common characteristics for all the regions because the magnetic field strength and inclination vary significantly according to umbrae or penumbrae in the sunspots. L3, L7, and L20 are situated almost within penumbrae because the continuum intensity is relatively large (0.6–1.0). For such regions, the magnetic field strength is about 1.0–1.5 kG, and the inclination is 20°–60°. The large magnetic inclination observed in L3 and L20 corresponds to the magnetic field in an outer penumbra. L25 is in an umbra; the continuum intensity is significantly smaller (<0.5) with large field strength (>2 kG), and the filling factor is almost unity. As expected, all the footpoint regions in sunspots have larger filling factors than the NS moss regions.

6. COMPARISON BETWEEN THE HOT AND COOL LOOPS

We sum the histograms of the magnetic parameters for the moss regions and the loop footpoint regions and present the summed histograms in Figure 10. The NS regions and the EFRs are distinctly shown in the upper histograms for the moss regions. The footpoint regions of the cool loops in the sunspots

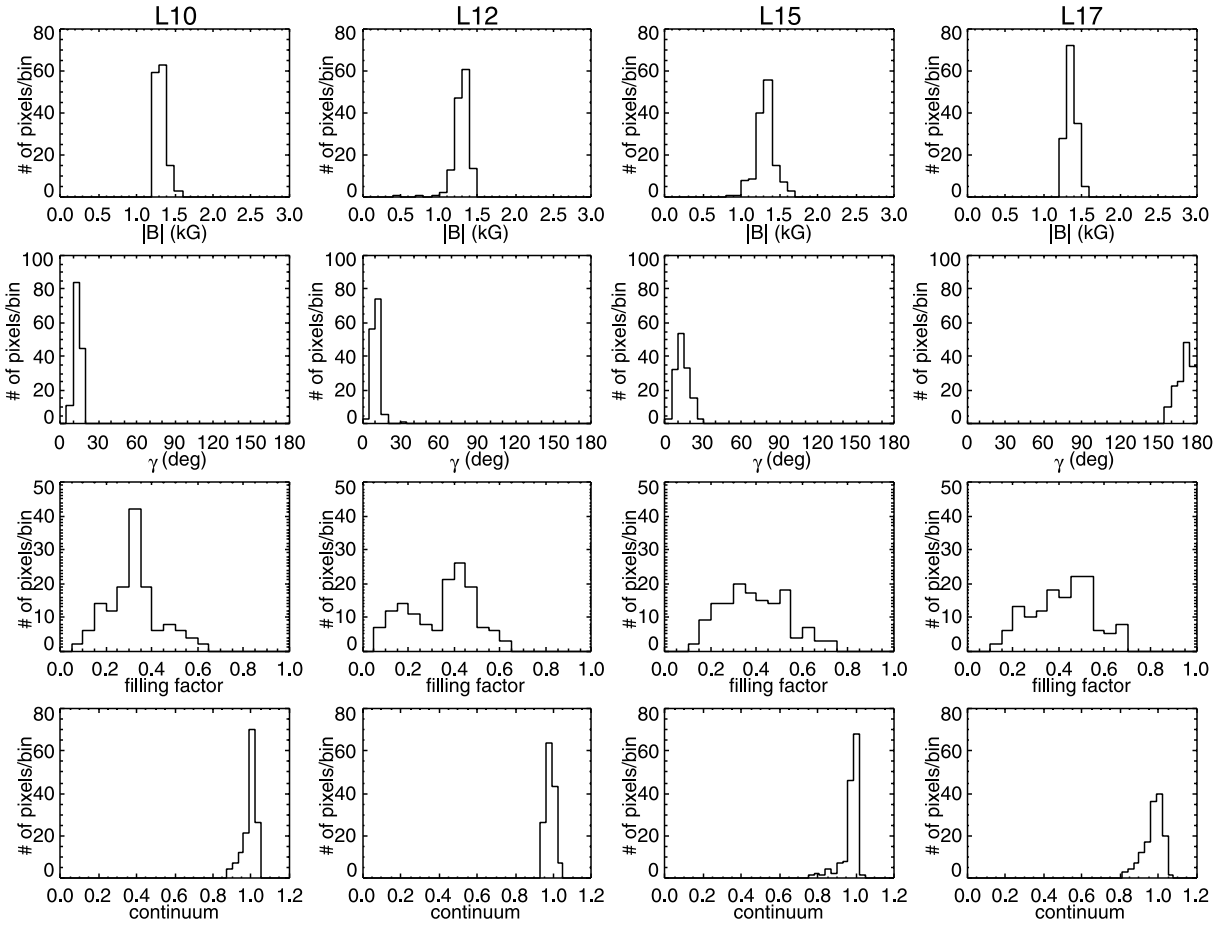


FIG. 7.—Histograms of the magnetic field strength $|B|$ (*top row*), the magnetic field inclination γ (*second row*), the filling factor f (*third row*), and the continuum intensity I_c (*bottom row*) for the loop footpoint regions L10, L12, L15, and L17 in the NS area.

and the NS regions are distinguished in the lower histograms. When we compare the moss regions with the loop footpoint regions in the NS area, the magnetic field strength and the inclination exhibit similar distributions. A clear difference between the moss regions and the loop footpoint regions is discovered in the histograms showing the magnetic filling factor. The histogram of the moss regions has a large enhancement in the filling factor $f < 0.3$, whereas the histogram of the loop footpoint regions has a depletion in $f < 0.3$, and its peak is situated at around $f \sim 0.4$. If we include the footpoint regions in the sunspots, in which there are pixels where the field strength is greater than 2.0 kG and the inclination is greater than 30°, the tendency is more robust; the magnetic filling factor in the loop footpoint regions is larger than that in the NS moss regions. The moss regions in NS regions and EFRs have different properties, as described in § 4. Indeed, if we include the moss regions with EFRs, there appears to be a tail component in the filling factor histogram. Magnetic properties of both regions are summarized in Table 5.

We have shown that the magnetic filling factor is an important property to distinguish the hot and cool loops. In order to know whether the lower magnetic filling factor is a sufficient condition to make the hot coronal loops and the moss, we investigate how large a fraction of the area observed with the ASP is covered by the moss (i.e., footpoints of the hot loops) and the footpoints of the cool loops for a given filling factor. The result

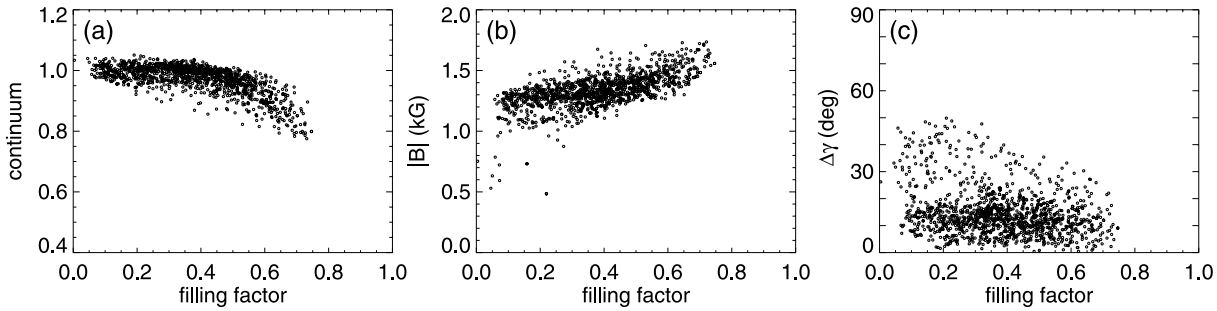


FIG. 8.—Scatter plots of (*a*) the continuum intensity I_c, (*b*) the magnetic field strength $|B|$, and (*c*) the magnetic inclination $\Delta\gamma$ as a function of the magnetic filling factor f for the loop footpoint regions in the NS area, where $\Delta\gamma = \gamma$ for $\gamma < 90°$ and $\Delta\gamma = (180° - \gamma)$ for $\gamma > 90°$.

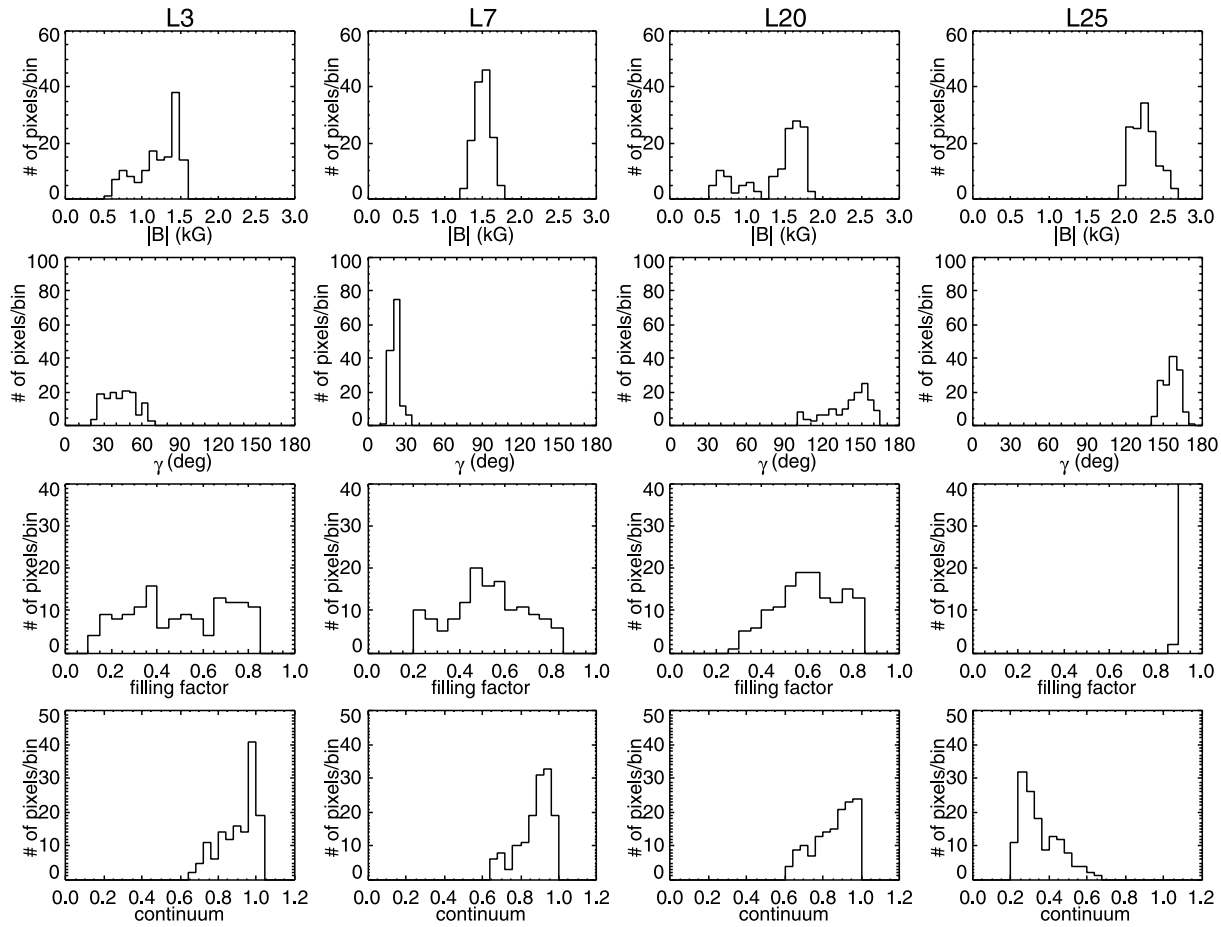


FIG. 9.—Same as Fig. 7, but for the footpoint regions in the sunspots L3, L7, L20, and L25 (*left to right*).

is shown in Figure 11. The area of the moss regions and the footpoint regions is defined in § 3. The moss regions occupy about 30% of the area in which the filling factor is from 0.2 to 0.4. Although the percentage depends slightly on the method employed in the extraction of the moss and the footpoint regions, over half of the area with $f \sim 0.2-0.4$ does not have the moss or cool loops in the *TRACE* image. The magnetic filling factor in the photosphere is one of the important parameters for the hot loops but is not a sufficient condition. Some yet-unknown conditions are necessary to make the hot loops in addition to the low magnetic filling factor.

We cannot obtain the magnetic parameters for the pixels for which the degree of polarization is lower than 0.4%. The magnetic filling factor is proportional to the degree of polarization for the same magnetic field strength and inclination. Figure 12 shows the scatter plot of the filling factor as a function of the

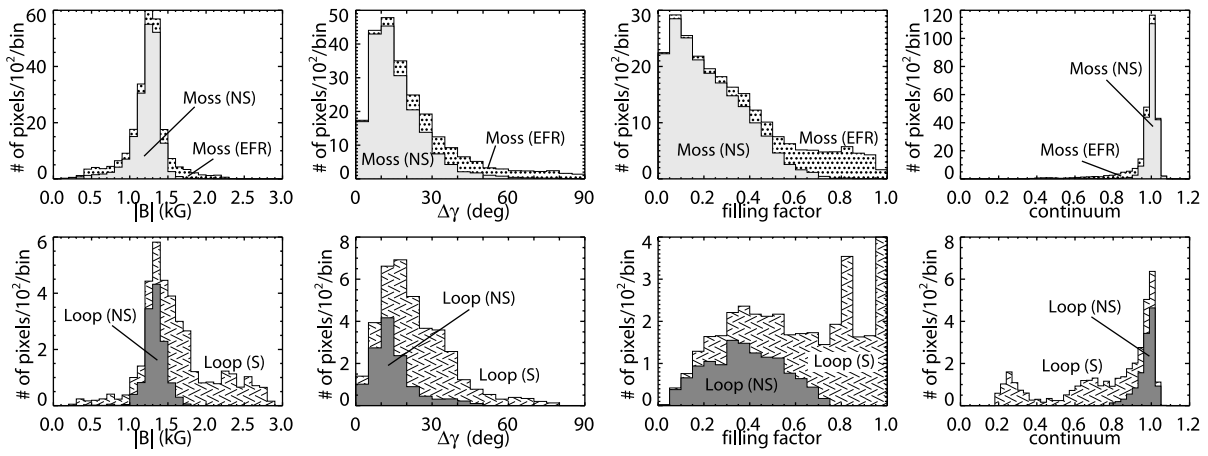


FIG. 10.—Histograms for the moss regions (*top*) and the footpoint regions of the cool loops (*bottom*). The moss regions in NS regions and those associated with the EFR are distinguished by the different shading patterns in the top histograms. The footpoint regions of the cool loops in the sunspots (S) and the NS regions are distinguished in the bottom histograms. The figure shows the magnetic field strength $|B|$, the magnetic field inclination $\Delta\gamma$, the magnetic filling factor f, and the continuum intensity I_c (*left to right*).

TABLE 5
MAGNETIC PROPERTIES IN THE MOSS AND FOOTPOINT REGIONS

	Moss (Hot Loops)		Cool Loops	
Property	NS	EFR	NS	Sunspot
Strength	1.2 kG	0.5–2.2 kG	1.3 kG	1.3–2.8 kG
Inclination	$<30^\circ$	0°–90°	$<30^\circ$	$<60^\circ$
Filling factor	0.05–0.3	0.3–0.9	0.2–0.6	0.5–1.0

degree of polarization. The filling factor, f, is well correlated with the degree of polarization, p, and is expressed as the linear relation

$$f = 0.0 + 9.6p. \quad (6)$$

Using this relation, the lower limit (0.4%) in the degree of polarization used in the Stokes inversion corresponds to $f \simeq 0.04$. Thus, we cannot measure the magnetic fields for the pixels with a filling factor less than 0.04. In Figure 11 a slight decrease in the percentage of the area covered with the moss can be seen as the filling factor becomes smaller, but whether the moss region is associated with such a small filling factor (less than 0.04) remains unknown in this analysis. A filling factor smaller than 0.04 is probably caused by scattering from larger values. The uncertainties of the inferred filling factors are estimated in the Appendix. Since we do not see the hot loops in the quiet Sun, which presumably has magnetic filling factors as low as 0.01 (Socas-Navarro & Sánchez Almeida 2002), there has to be a truncation in the distribution function of the filling factor for the moss regions at 0.01–0.1.

Figure 11 also shows that the footpoint regions of the cool loops only cover less than 10% of the area with $f > 0.4$. This implies that neither moss nor loops are observed with *TRACE* in such higher filling factor regions except the EFR. In addition to the filling factor at the footpoints, an additional condition may control the coronal heating rate in the high filling factor area. Since the analysis windows (5″) used here are larger than the width of the cool loops, there is a possibility that we miss fine magnetic structures localized at the footpoints of the cool loops.

7. SUMMARY AND DISCUSSION

We discover that the most significant difference between the hot loops and the cool ones is the magnetic filling factor of their footpoints. In the nonsunspot regions, the moss structure, i.e., the footpoint of the hot loops, is essentially observed in the area in which the filling factor is small ($f < 0.4$), and the cool loops are associated with the region of relatively high filling factor. The magnetic properties (field strength, inclination, and filling factor) observed in the moss regions correspond to those of plages described in Martinez Pillet et al. (1997). Almost all footpoint regions of the cool loops are found to be associated with pores or sunspots. The exception is the moss associated with the emerging flux. Those regions have larger filling factors, and the magnetic fields in the regions are significantly inclined with respect to the normal of the photosphere.

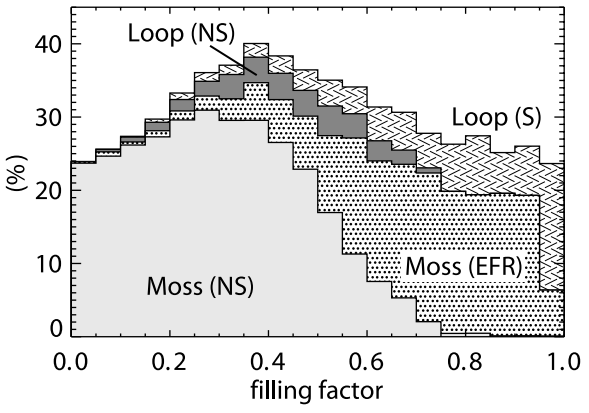


FIG. 11.—Percentage of the area covered with the moss and loop footpoint regions as a function of the magnetic filling factor. Shading patterns similar to those in Fig. 10 are used to distinguish the moss regions (NS and EFR) and the footpoint regions of the cool loops (S and NS).

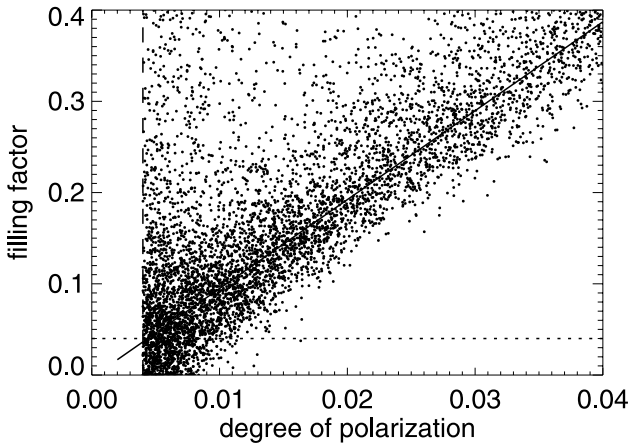


FIG. 12.—Scatter plot of the magnetic filling factor as a function of the degree of polarization [$p = (Q^2 + U^2 + V^2)^{1/2}/I$ integrated over the 6302.5 Å line]. The vertical dashed line indicates the lower limit of the polarization fraction (0.4%) that is adopted in the Stokes inversion. The solid line shows the relation of eq. (6).

The photospheric magnetic fields concentrate at around 1–1.5 kG, and their orientation is nearly vertical to the surface, as shown in Figure 10. We assume that solar magnetic flux on the photosphere consists of magnetic elements of the same strength (e.g., Stenflo & Harvey 1985; Solanki 1993). The magnetic filling factor is, therefore, proportional to the surface number density of these magnetic elements if we assume that the spatial size of those magnetic elements is the same. The low magnetic filling factor observed in the moss regions corresponds to the low number density of the magnetic elements, as shown in Figure 13*a*. On the other hand, the number density is larger for the footpoint regions of the cool loops, as shown in Figure 13*b*.

The difference between the hot and cool loops appears to be produced by the difference in the heating energy. That is, the hot loops require more energy than the cool loops. Here we discuss why the dispersed magnetic elements in the photosphere are the cause of the large heating energy required by the hot loops.

7.1. *Mobility of Magnetic Elements*

The magnetic elements are believed to correspond to the photospheric bright points in the G band (Berger & Title 2001). The velocity of the magnetic elements is around 1 km s^{-1} for isolated bright points (Nisenson et al. 2003) and around 0.4 km s^{-1} for clusters of bright points (van Ballegooijen et al. 1998). The motion of the magnetic elements in a pore is studied by Sobotka et al. (1999) using the umbral dot, which is the bright pointlike structure in a pore and an umbra. They show that the velocity of the umbral dot in a pore is around 0.2 km s^{-1}, apparently slower than that of the photospheric bright points. These observations imply that the motions of each element would be suppressed when the magnetic elements are concentrated.

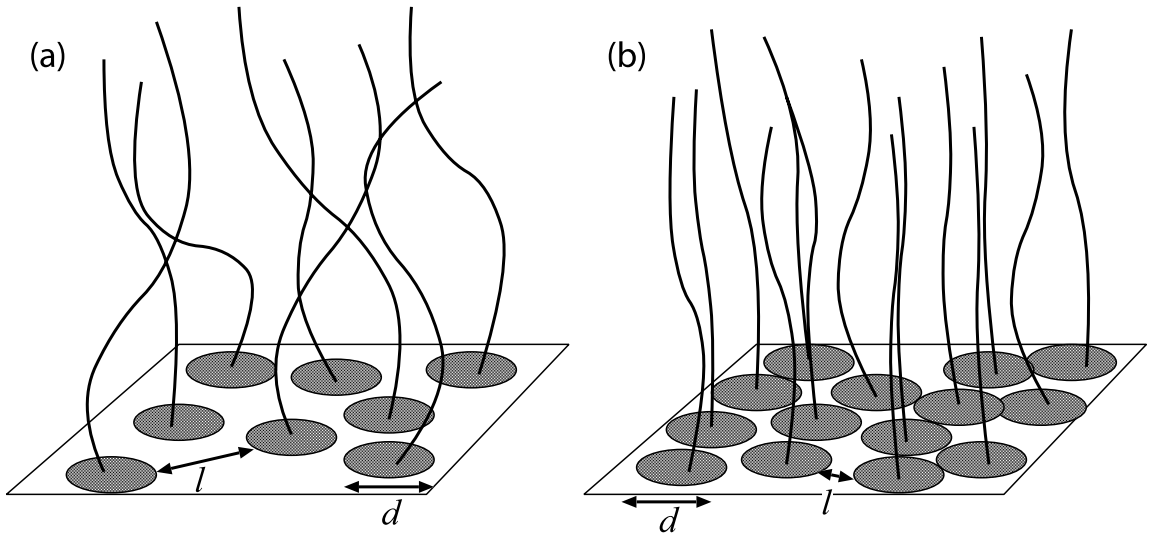


FIG. 13.—Schematic illustration of footpoint regions of (*a*) hot and (*b*) cool loops. Each shaded circle represents a magnetic element with a diameter of *d*.

The distance that the magnetic elements can be freely moved by photospheric motion would be affected by the magnetic filling factor. We examine the mean free path of a magnetic element. The mean free path here means the distance over which a magnetic element travels, on average, between two successive collisions with other magnetic elements. We suppose that the magnetic elements are uniformly distributed over the photosphere. In this case, the filling factor f is given by

$$f = \frac{1}{4}\pi n d^2, \tag{7}$$

where d is the diameter of each magnetic element, and n is the number of magnetic elements per unit area. Each magnetic element is assumed to travel because of photospheric motion until the distance between the centers of two elements becomes less than $d/2$. When the mean free path of a magnetic element is l, one magnetic element sweeps over the area $dl + \frac{1}{4}\pi d^2$ before collision. The number of magnetic elements in this area is, by definition, one; that is,

$$n\left(dl + \frac{1}{4}\pi d^2\right) = 1. \tag{8}$$

From equations (7) and (8), the mean free path l can be expressed as a function of the filling factor f,

$$l = \frac{\pi d}{4}\left(\frac{1}{f} - 1\right). \tag{9}$$

Figure 14 shows the mean free path l as a function of the filling factor f, where the diameter of the magnetic element d is assumed to be 100 km corresponding to 0.″14 (e.g., Topka et al. 1992). When the filling factor is 0.1 and 0.5, the mean free path is around 700 and 80 km, respectively. This means that the mobility of a magnetic element is suppressed in the region in which the magnetic filling factor is large. This exercise provides a rough estimate of the mean free path of a magnetic element. In the actual photosphere, the magnetic elements are moved by their interaction with convection. When the mean free path given by the above equation becomes large enough, the path might be bounded by the spatial scale of the convection ($l_c \simeq 1000$ km, indicated by the horizontal dashed line in Fig. 14). The mean free path is larger than $l_c \simeq 1000$ km when the magnetic filling factor f is less than 0.07 in equation (9). The simple estimation made here would be valid only for $f > 0.07$. Furthermore, a magnetic element may be broken before collision with another element when the mean free path is large. The lifetime of the G-band bright points is typically 10 minutes (Berger et al. 1998). The path of the bright points during their lifetime is around 600 km when the velocity is 1 km s^{-1}.

7.2. *Energy Flux into the Corona*

Braiding of magnetic field lines as a result of motion of the magnetic elements in the photosphere makes current sheets in the corona and results in rapid dissipation of the magnetic energy to heat it (Parker 1972, 1983). The mechanical work done for the magnetic fields by the photospheric motion of the magnetic elements can be written as

$$F = \frac{1}{4\pi} f v_t B_n B_t, \tag{10}$$

where v_t is the horizontal component of the velocity and B_n and B_t are the normal and horizontal components of the magnetic fields, respectively. Here we neglect the energy flux by the flux emergence, because the magnetic inclination at the loop footpoints is nearly vertical to the surface. Since B_n is not very

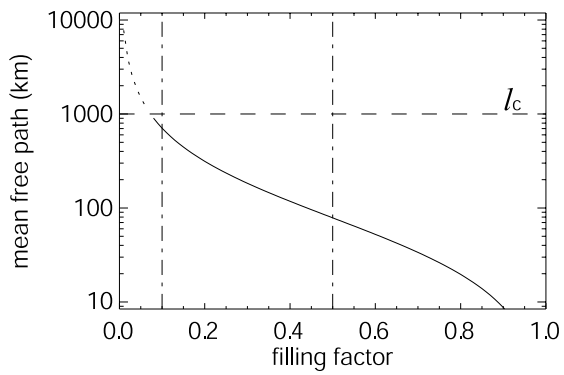


FIG. 14.—Mean free path of the magnetic elements as a function of the magnetic filling factor (see eq. [9]).

different between the hot and cool loops, as shown in Figure 10, the energy flux F depends on f, v_t, and B_t. The lower filling factor observed in the moss regions makes the energy input smaller. However, v_t appears to anticorrelate with the filling factor, and B_t becomes large because of the larger mean free path of the magnetic elements. The horizontal component of the magnetic field B_t generated by the photospheric motion is roughly estimated as

$$B_t = B_n \frac{l}{L} \tag{11}$$

when the mean free path of the magnetic elements l and the loop length L are given. Using equations (9), (10), and (11), the energy flux F can be expressed as a function of the magnetic filling factor f,

$$F = \frac{v_t d}{16L} B_n^2 (1 - f). \tag{12}$$

This equation shows that B_t generated by the high mobility has a possibility of providing the larger energy input when the magnetic filling factor is small (see Fig. 13). When $L \sim 10^5$ km, $B_n = 1.2$ kG, and $d = 100$ km, the energy flux $F \simeq 8 \times 10^6$ ergs cm^{-2} s^{-1} can be obtained using the magnetic properties observed in the moss regions, $v_t \simeq 1$ km s^{-1} and $f \simeq 0.1$. On the other hand, the properties in a pore, $v_t \simeq 0.2$ km s^{-1} and $f \simeq 0.5$, lead to the energy flux $F \simeq 1 \times 10^6$ ergs cm^{-2} s^{-1}, 1 order of magnitude lower than that of the moss regions. This estimate of the energy flux implies that the differences in both the mobility of the magnetic elements and the effectiveness of the braiding action can generate different heating input to the corona, leading to the difference between the hot and cool loops.

The photospheric motion of magnetic elements, v_t, cannot be directly obtained from this ASP observation, although its significant contribution to the energy input is implied in equation (12). As we described in § 6, over half of the region with the low filling factor does not have either the hot loops or the cool ones. We do not know the sufficient condition in the photosphere to cause the coronal loops. We point out that, as a first step, not only measurements of magnetic fields but simultaneous measurements of photospheric velocity fields have to be performed in order to investigate the sufficient condition for the hot and cool loops.

According to equation (12), the energy flux provided from the sunspot is too small to heat the cool loops, because the magnetic filling factor in the sunspot is nearly unity (as described in § 5.2) and the photospheric motion seems to be strongly suppressed there (Sobotka et al. 1997). This implies that the energy input by braiding of magnetic field lines is not available at the footpoints of the cool loops emanating from the sunspots. Since there are cool loops whose other footpoints are in nonsunspot areas, it is still possible that the heating energy for the cool loops is supplied from the other footpoints in the nonsunspot areas. There is also a possibility that an alternative mechanism of energy input might be necessary to account for such cool loops.

The energy input in the quiet-Sun corona is 1–2 orders of magnitude smaller than that in the active region corona (e.g., Withbroe & Noyes 1977). Socas-Navarro & Sánchez Almeida (2002) investigated the magnetic properties of the quiet Sun and showed that the magnetic filling factor was as low as 0.01 while the magnetic field strength was over 1 kG. The expression of equation (12) may not be valid for an area with such a low filling factor because the magnetic elements cannot be transported by the convective motion over a distance longer than the spatial scale of the convection ($l_c \sim 1000$ km). When the mean free path of the magnetic elements is constant for the region with the low filling factor, equation (10) indicates that the energy flux into the corona is proportional to the magnetic filling factor if the photospheric motion is not very different. Thus, the lower heating rate in the quiet Sun could be explained simply by the lower magnetic filling factor.

We are grateful to M. Kubo, T. Shimizu, and B. W. Lites for providing an opportunity to use the ASP data. We also acknowledge an anonymous referee for his/her helpful comments.

APPENDIX

UNCERTAINTIES OF THE FILLING FACTORS

Here we estimate the uncertainties in the derived filling factors using two independent methods. The inversion code described in § 2.2 yields formal 1 σ uncertainties of its own fitting parameters for each set of Stokes profiles at each point in the observed area (Lites et al. 1993, 1994). These errors represent the allowed range of fluctuation of each parameter that is permitted by the fit to the observed

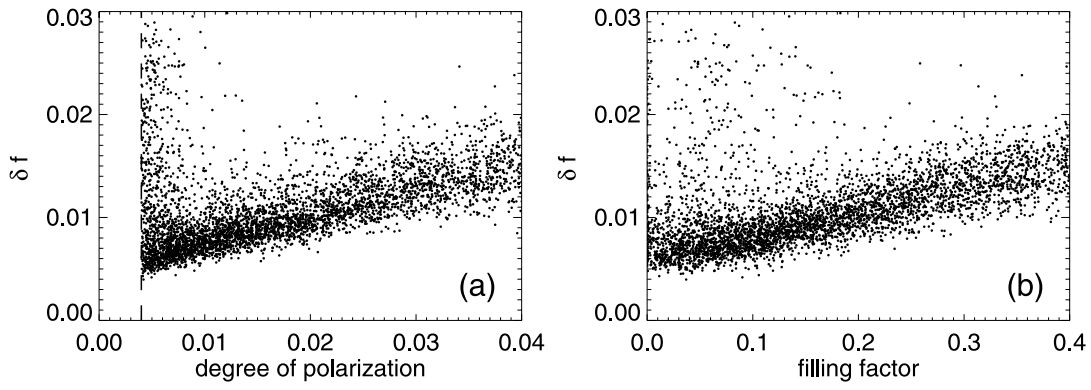


FIG. 15.—Uncertainties (1 σ) of the filling factors, δf, returned from the inversion code. They are represented as a function of (*a*) the degree of polarization and (*b*) the filling factor; each pixel is represented by a dot.

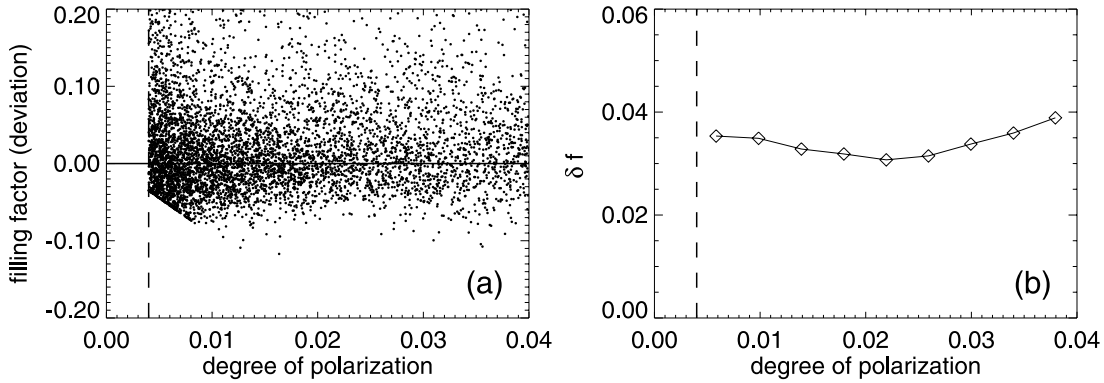


FIG. 16.—(*a*) Deviations of the filling factors from the linear relation expressed by eq. (6), and (*b*) their standard deviations as a function of p.

data. Figure 15 shows the 1 σ errors in the magnetic filling factor, δf, as a function of the degree of polarization, p (Fig. 15*a*), and the inferred values of the magnetic filling factor, f (Fig. 15*b*). The errors δf are typically around 0.01 and increase slightly with increasing p or f. There are some pixels that have relatively large errors ($\sim$0.03) near $p \sim 0.4\%$, which is the lower limit of the Stokes inversion.

In addition to the formal 1 σ errors in the least-squares fit, we also measure an error of the inferred filling factor from the deviation of data points from the linear relation between the filling factor and the degree of polarization illustrated in Figure 12. Figure 16*a* shows deviations of the filling factors from the relation given by equation (6) at each pixel. We can see that the deviations are larger near the lower limit of p (0.4%). We make histograms of the deviations of f at an interval of 0.4% as a function of p. The histograms are then fitted to a Gaussian profile, and the standard deviations are calculated from the fitted Gaussian profile. Figure 16*b* shows the derived standard deviations as a function of p. The errors are between 0.03 and 0.04 in $p < 4\%$. Since the linear relation between p and f holds only for the same magnetic field strength and inclination, variation of the field strength and inclination makes the regression worse. The relatively larger errors in the filling factor compared with the formal errors shown in Figure 15 are most likely due to this variation of the field strength and inclination. The uncertainties of the filling factors shown in Figure 16*b* are regarded as an upper limit.

REFERENCES

Antiochos, S. K., Karpen, J. T., DeLuca, E. E., Golub, L., & Hamilton, P. 2003, ApJ, 590, 547
Aschwanden, M. J., Nightingale, R. W., & Alexander, D. 2000, ApJ, 541, 1059
Aschwanden, M. J., Schrijver, C. J., & Alexander, D. 2001, ApJ, 550, 1036
Berger, T. E., De Pontieu, B., Fletcher, L., Schrijver, C. J., Tarbell, T. D., & Title, A. M. 1999, Sol. Phys., 190, 409
Berger, T. E., Loefdahl, M. G., Shine, R. S., & Title, A. M. 1998, ApJ, 495, 973
Berger, T. E., & Title, A. M. 2001, ApJ, 553, 449
Delaboudinière, J. P., et al. 1995, Sol. Phys., 162, 291
Elmore, D. F., et al. 1992, Proc. SPIE, 1746, 22
Falconer, D. A., Moore, R. L., Porter, J. G., Gary, G. A., & Shimizu, T. 1997, ApJ, 482, 519
Fisher, G. H., Longcope, D. W., Metcalf, T. R., & Pevtsov, A. A. 1998, ApJ, 508, 885
Fletcher, L., & de Pontieu, B. 1999, ApJ, 520, L135
Handy, B. N., et al. 1999, Sol. Phys., 187, 229
Kano, R., & Tsuneta, S. 1995, ApJ, 454, 934
———. 1996, PASJ, 48, 535
Keppens, R., & Martinez Pillet, V. 1996, A&A, 316, 229
Kubo, M., Shimizu, T., & Lites, B. W. 2003, ApJ, 595, 465
Leka, K. D., & Skumanich, A. 1998, ApJ, 507, 454
Lenz, D. D., Deluca, E. E., Golub, L., Rosner, R., & Bookbinder, J. A. 1999, ApJ, 517, L155
Lites, B. W. 1996, Sol. Phys., 163, 223
———. 2002, ApJ, 573, 431
Lites, B. W., Elmore, D. F., Seagraves, P., & Skumanich, A. P. 1993, ApJ, 418, 928
Lites, B. W., Low, B. C., Martinez Pillet, V., Seagraves, P., Skumanich, A., Frank, Z. A., Shine, R. A., & Tsuneta, S. 1995, ApJ, 446, 877
Lites, B. W., Martinez Pillet, V., & Skumanich, A. 1994, Sol. Phys., 155, 1
Lites, B. W., & Skumanich, A. 1990, ApJ, 348, 747
Lites, B. W., Skumanich, A., & Martinez Pillet, V. 1998, A&A, 333, 1053
Martens, P. C. H., Kankelborg, C. C., & Berger, T. E. 2000, ApJ, 537, 471
Martinez Pillet, V., Lites, B. W., & Skumanich, A. 1997, ApJ, 474, 810
Nagata, S., et al. 2003, ApJ, 590, 1095
Nisenson, P., van Ballegooijen, A. A., de Wijn, A. G., & Sütterlin, P. 2003, ApJ, 587, 458
Ogawara, Y., Takano, T., Kato, T., Kosugi, T., Tsuneta, S., Watanabe, T., Kondo, I., & Uchida, Y. 1991, Sol. Phys., 136, 1
Pallavicini, R., Vaiana, G. S., Tofani, G., & Felli, M. 1979, ApJ, 229, 375
Parker, E. N. 1972, ApJ, 174, 499
———. 1983, ApJ, 264, 642
Priest, E. R., Foley, C. R., Heyvaerts, J., Arber, T. D., Culhane, J. L., & Acton, L. W. 1998, Nature, 393, 545
Priest, E. R., Foley, C. R., Heyvaerts, J., Arber, T. D., Mackay, D., Culhane, J. L., & Acton, L. W. 2000, ApJ, 539, 1002
Reale, F., & Peres, G. 2000, ApJ, 528, L45
Rosner, R., Tucker, W. H., & Vaiana, G. S. 1978, ApJ, 220, 643
Sánchez Almeida, J., Domínguez Cerdeña, I., & Kneer, F. 2003, ApJ, 597, L177
Scherrer, P. H., et al. 1995, Sol. Phys., 162, 129
Schmieder, B., Rust, D. M., Georgoulis, M. K., Démoulin, P., & Bernasconi, P. N. 2004, ApJ, 601, 530
Schrijver, C. J., et al. 1999, Sol. Phys., 187, 261
Semel, M., & Skumanich, A. 1998, A&A, 331, 383
Skumanich, A., & Lites, B. W. 1987, ApJ, 322, 473
Skumanich, A., Lites, B. W., Martinez Pillet, V., & Seagraves, P. 1997, ApJS, 110, 357
Sobotka, M., Brandt, P. N., & Simon, G. W. 1997, A&A, 328, 689
Sobotka, M., Vázquez, M., Bonet, J. A., Hanslmeier, A., & Hirzberger, J. 1999, ApJ, 511, 436
Socas-Navarro, H., & Sánchez Almeida, J. 2002, ApJ, 565, 1323
Solanki, S. K. 1993, Space Sci. Rev., 63, 1
Stenflo, J. O., & Harvey, J. W. 1985, Sol. Phys., 95, 99
Topka, K. P., Tarbell, T. D., & Title, A. M. 1992, ApJ, 396, 351
Tsuneta, S., et al. 1991, Sol. Phys., 136, 37
Vaiana, G. S., Zombeck, M., Krieger, A. S., & Timothy, A. F. 1976, Ap&SS, 39, 75
van Ballegooijen, A. A., Nisenson, P., Noyes, R. W., Löfdahl, M. G., Stein, R. F., Nordlund, Å., & Krishnakumar, V. 1998, ApJ, 509, 435
Vourlidas, A., Bastian, T. S., & Aschwanden, M. J. 1997, ApJ, 489, 403
Winebarger, A. R., Warren, H. P., & Mariska, J. T. 2003, ApJ, 587, 439
Withbroe, G. L., & Noyes, R. W. 1977, ARA&A, 15, 363
Yashiro, S., & Shibata, K. 2001, ApJ, 550, L113
Yoshida, T., & Tsuneta, S. 1996, ApJ, 459, 342
Yoshida, T., Tsuneta, S., Golub, L., Strong, K., & Ogawara, Y. 1995, PASJ, 47, L15